J. Fluid Mech. (2024), *vol*. 979, A45, doi:10.1017/jfm.2023.1101

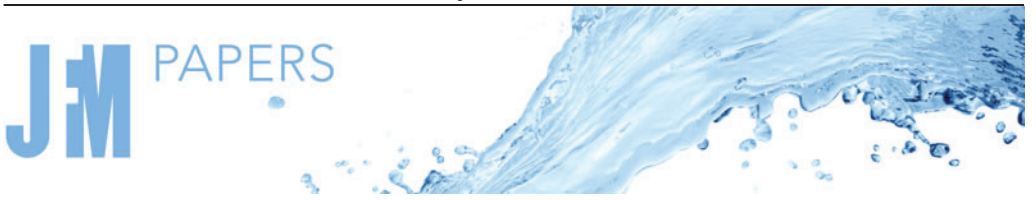

Twin forces: similarity between rotation and stratification effects on wall turbulence

Shengqi Zhang[1],† **and Chao Sun**[2,3]

[1]Eastern Institute for Advanced Study, Eastern Institute of Technology, Ningbo 315201, PR China

[2]Center for Combustion Energy, Key Laboratory for Thermal Science and Power Engineering of MoE, and Department of Energy and Power Engineering, Tsinghua University, Beijing 100084, PR China

[3]Department of Engineering Mechanics, School of Aerospace Engineering, Tsinghua University, Beijing 100084, PR China

(Received 17 August 2023; revised 11 December 2023; accepted 20 December 2023)

Can the similarity between rotation and stratification provide quantitative predictions for complex turbulence? In this work, we focus on plane Couette turbulence as the background flow, which allows us to eliminate the key differences between Rayleigh–Bénard and Taylor–Couette turbulence, and facilitates a quantitative mapping across many complex turbulent systems involving rotation, stratification and curvature effects. To characterize the separated or coupled effects of rotation and stratification, we introduce an overall Richardson number Ri_χ which is the sum of the Coriolis Richardson number Ri_θ and the buoyancy Richardson number Ri_T. When the Prandtl number $Pr = 1$, the heat and inertial-frame momentum transport almost coincide and mainly depend on Ri_χ and the Reynolds number, regardless of the specific ratio between Ri_θ and Ri_T. When Pr varies, the weighted average Nu_χ of the transport coefficients can still remain approximately invariant in most cases. Furthermore, the large-scale structures in purely rotating and purely stratified cases exhibit strikingly similar features. These findings not only indicate a more reasonable analogy for the ultimate Taylor–Couette turbulence but also pave the way for developing new predictive models for natural and industrial processes.

Key words: Bénard convection, rotating turbulence, stratified turbulence

1. Introduction

Rotating and stratified flows are prevalent in various turbulent systems, ranging from the Earth's atmosphere (Wyngaard 1992; Hartmann, Moy & Fu 2001) and celestial bodies (Young & Read 2017; Schumacher & Sreenivasan 2020) to turbomachinery (Han 2018; You *et al.* 2018). In celestial bodies, for instance, the Coriolis force significantly influences

† Email address for correspondence: shengqizhang@eias.ac.cn

buoyancy-driven flows (Wyngaard 1992; Young & Read 2017; Schumacher & Sreenivasan 2020), whereas in high-temperature turbines, the buoyancy force has a substantial impact on rotating flows (Han 2018; You *et al.* 2018). The coupling effects of the Coriolis and buoyancy forces are perfectly illustrated in the Earth's global atmospheric circulation with Hadley, Ferrel and polar cells (Lutgens, Tarbuck & Tasa 2007). Therefore, it is essential to consider both the isolated and combined effects of rotation and stratification in these systems.

A possible approach to better understand these complex effects is the analogy between rotating wall turbulence and buoyancy-driven turbulence (Jeffreys 1928; Bradshaw 1969; Veronis 1970; Lezius & Johnston 1976; Tanaka *et al.* 2000; Busse 2012; Ostilla-Mónico *et al.* 2014; Brauckmann, Eckhardt & Schumacher 2017; Zhang *et al.* 2019; Eckhardt, Doering & Whitehead 2020; Brethouwer 2021; Zhang, Xia & Chen 2022). One of the most well-known examples is the analogy between Taylor–Couette flow (Taylor 1923; van Gils *et al.* 2011; Huisman *et al.* 2012; Grossmann, Lohse & Sun 2016; Zhu *et al.* 2018) and Rayleigh–Bénard convection (Kraichnan 1962; Ahlers, Grossmann & Lohse 2009; Lohse & Xia 2010; Grossmann & Lohse 2011; Zhu *et al.* 2019; Wang, Zhou & Sun 2020; Jiang *et al.* 2022), which are referred to as 'the twins of turbulence research' by Busse (2012). These two systems exhibit similar ultimate scaling of heat or angular momentum transport and Reynolds number (van Gils *et al.* 2011; Huisman *et al.* 2012; Zhu *et al.* 2018, 2019; Jiang *et al.* 2022), and their turbulent statistics and flow structures are also similar when their transport coefficients (angular momentum for Taylor–Couette and heat for Rayleigh–Bénard) are chosen to be consistent (Brauckmann *et al.* 2017). However, the analogy is found to only hold in a qualitative way, particularly for the prediction of the transition parameters of the different systems. This is mainly caused by two differences between these two systems. First, it is easier for the Taylor–Couette system to have a turbulent boundary layer due to wall shear, while the Rayleigh–Bénard system can only achieve boundary layer transition indirectly through the buoyancy effect (Grossmann *et al.* 2016). Second, although both the ideal Taylor–Couette system (infinitely long cylinders) and the ideal Rayleigh–Bénard system (infinitely large plates) are statistically homogeneous in the directions perpendicular to the wall-normal direction, they are very different in isotropy. Statistically, the Rayleigh–Bénard system exhibits horizontal isotropy, while the Taylor–Couette system is not isotropic in the azimuthal-axial hyperplanes even in the limit of vanishing curvature.

Fortunately, in many realistic stratified flows, stratification is coupled with wall shear (Prandtl 1932; Obukhov 1946; Monin & Obukhov 1954; Kader & Yaglom 1990; Deusebio, Caulfield & Taylor 2015; Pirozzoli *et al.* 2017; Zhou, Taylor & Caulfield 2017; Haghshenas & Mellado 2019; Blass *et al.* 2020, 2021), effectively eliminating the two primary differences. To be specific, adding a mean shear to the Rayleigh–Bénard system not only makes it easier to achieve boundary layer transition, but also breaks the horizontal isotropy. Therefore, investigating the effects of rotation and stratification in wall-sheared flows can help upgrade the qualitative analogy into a quantitative prediction approach.

The analogy between two systems can be further extended to the analogy between the rotation and stratification effect, and also the analogy between heat and momentum transfer in rotating stratified wall turbulence. These analogies can provide a more comprehensive understanding of the dynamics of complex wall turbulence. Since the limiting case of Taylor–Couette flow with vanishing curvature is the spanwise rotating plane Couette flow (Faisst & Eckhardt 2000; Dubrulle *et al.* 2005; Brauckmann, Salewski & Eckhardt 2016), and the Rayleigh–Bénard convection with wall shear can be called stratified plane Couette flow, it is straightforward to

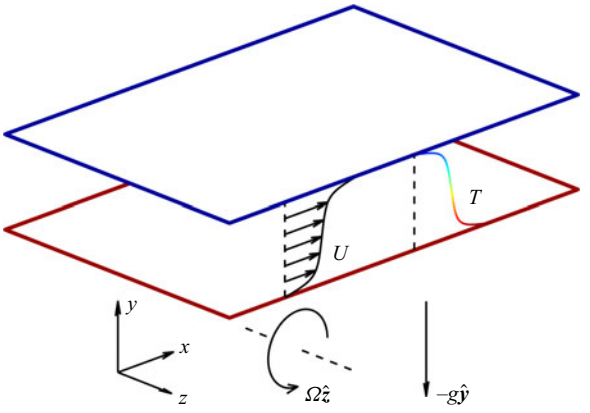

Figure 1. Sketch of spanwise rotating stratified plane Couette flow.

choose plane Couette turbulence as the background flow to investigate both rotation and stratification effects. In addition, essentially identical boundary conditions of velocity and temperature can be applied to plane Couette turbulence, making it convenient to examine the analogy between heat and momentum transfer in the same case. The analogy between the rotation and stratification effect can be examined through the comparison between two cases with different combinations of rotation and stratification.

In this work, we investigate the turbulence statistics and large-scale flow structures in plane Couette turbulence subject to rotation or stratification, or combinations of both effects. The basic equations and mathematical basis of thermal analogy, followed by redefined physical parameters and our theoretical conjectures, are introduced in § 2. The conjectures are then examined and rectified with previous and newly obtained numerical simulation results in § 3. Finally, the present work will be summarized in § 4.

2. Governing equations and theoretical conjectures

2.1. *Original equations*

As shown in figure 1, the x, y and z axes with corresponding unit vectors $\hat{\boldsymbol{x}}$, $\hat{\boldsymbol{y}}$ and $\hat{\boldsymbol{z}}$ represent the streamwise, wall-normal and spanwise directions, respectively. We denote the streamwise velocity and temperature difference between two walls as $[U]$ and $[T]$, the distance between the walls as H, the gravitational acceleration as $-g\hat{\boldsymbol{y}}$, the angular velocity as $\Omega\hat{\boldsymbol{z}}$, the thermal expansion coefficient as β, the kinematic viscosity as ν and thermal diffusion coefficient as α. The centrifugal buoyancy is not shown explicitly mainly because the effect of centrifugal force induced by the Earth's rotation is embedded in the shape of the Earth and locally measured values of gravitational acceleration. In addition, centrifugal buoyancy in a rapidly rotating Taylor–Couette device with a large radius ratio can serve as a wall-normal 'gravity' (Jiang *et al.* 2022). There are four independent control parameters: the Reynolds number $Re = [U]H/\nu$, the rotation number $R_\Omega = 2\Omega H/[U]$, the Rayleigh number $Ra = g\beta[T]H^3/\nu\alpha$ and the Prandtl number $Pr = \nu/\alpha$. Under the Boussinesq approximation (Boussinesq 1903), the non-dimensionalized basic equations

are as follows:

$$\boldsymbol{\nabla}\cdot\boldsymbol{u}=0, \tag{2.1a}$$

$$\frac{\partial \boldsymbol{u}}{\partial t}+\boldsymbol{u}\cdot\boldsymbol{\nabla}\boldsymbol{u}=-\boldsymbol{\nabla}p+\frac{1}{Re}\nabla^2\boldsymbol{u}+R_\Omega\boldsymbol{u}\times\hat{\boldsymbol{z}}+\frac{Ra}{Re^2Pr}T\hat{\boldsymbol{y}}, \tag{2.1b}$$

$$\frac{\partial T}{\partial t}+\boldsymbol{u}\cdot\boldsymbol{\nabla}T=\frac{1}{RePr}\nabla^2T, \tag{2.1c}$$

where the boundary conditions are $\boldsymbol{u}|_{y=\pm0.5}=\pm0.5\hat{\boldsymbol{x}}$ and $T|_{y=\pm0.5}=\mp0.5$.

2.2. *Thermal analogy*

For spanwise rotating shear flows, a variable transformation (Tanaka *et al.* 2000; Zhang *et al.* 2019) indicates that the Coriolis force has a buoyancy-like effect on the wall-normal velocity. We can extend this variable transformation to the present rotating stratified system, which reveals a striking similarity between the effects of the Coriolis and buoyancy forces characterized respectively by R_Ω and Ra. Specifically, by defining $\theta=(R_\Omega y-u)/(1-R_\Omega)$, the streamwise and wall-normal momentum equations can be expressed as follows (detailed derivations are shown in Appendix A):

$$\frac{\partial\theta}{\partial t}+\boldsymbol{u}\cdot\boldsymbol{\nabla}\theta=\frac{1}{1-R_\Omega}\frac{\partial\tilde{p}}{\partial x}+\frac{1}{Re}\nabla^2\theta, \tag{2.2a}$$

$$\frac{\partial v}{\partial t}+\boldsymbol{u}\cdot\boldsymbol{\nabla}v=-\frac{\partial\tilde{p}}{\partial y}+\frac{1}{Re}\nabla^2v+R_\Omega(1-R_\Omega)\theta+\frac{Ra}{Re^2Pr}T, \tag{2.2b}$$

where $\tilde{p}=p+R_\Omega^2y^2/2$. Notably, the boundary condition of θ coincides with that of the temperature T, and the streamwise component of the Coriolis force is absorbed into the convection term of θ. We observe that the transformed equations establish a close analogy between θ and a temperature/concentration field with Prandtl/Schmidt number being 1 and Rayleigh number being $Re^2R_\Omega(1-R_\Omega)$. An apparent difference between θ and a temperature/concentration field is that θ has a source term arising from the incompressible constraint on velocity. This is because the incompressible condition requires a full elimination of the divergence and wall-normal flux of $\partial\boldsymbol{u}/\partial t$ by the pressure gradient $\boldsymbol{\nabla}p$, whose streamwise component appears as a source term in the $\partial\theta/\partial t$ equation.

2.3. *Theoretical conjectures*

Taking inspiration from the transformed variables and equations, we propose parameter transformations for the rotation number and Rayleigh number. Based on previous research on sheared Rayleigh–Bénard convection at different Prandtl numbers (Blass *et al.* 2021), we define the buoyancy Richardson number Ri_T as Ra/Re^2 for $Pr\leq1$ and $RaPr/Re^2$ for $Pr>1$ (explained later in this subsection). The Coriolis Richardson number is defined as $Ri_\theta=R_\Omega(1-R_\Omega)$. In classical Taylor–Couette systems with fixed outer cylinder and radius ratio larger than $1/2$, the angular velocity of the characteristic rotating system does not exceed a quarter of the spatially averaged rotating-frame vorticity, resulting in $R_\Omega\leq0.5$ (Dubrulle *et al.* 2005; Brauckmann *et al.* 2016). We are focusing on the same R_Ω range, which ensures that there is a one-to-one mapping between $(Re, Pr, Ri_T, Ri_\theta)$ and (Re, Pr, Ra, R_Ω) in the present study. Correspondingly, we define the heat Nusselt number as $Nu_T=-d\langle T\rangle/\mathrm{d}y|_{\pm0.5}$ and the momentum Nusselt number as $Nu_\theta=-d\langle\theta\rangle/\mathrm{d}y|_{\pm0.5}$. It should be noted that Nu_θ characterizes the streamwise momentum transport in the inertial frame.

Furthermore, we define an overall Richardson number and the relative stratification-rotation difference as

$$Ri_\chi = Ri_T + Ri_\theta, \quad \gamma = \frac{Ri_T - Ri_\theta}{Ri_T + Ri_\theta}, \tag{2.3a,b}$$

which can replace Ri_T and Ri_θ when $Ri_\chi \neq 0$. Our choice of defining Ri_χ is motivated by our goal to unify the effects of the Coriolis and buoyancy forces, while γ quantifies the relative contributions of the two forces. More specifically, we expect that Ri_χ consists of $50(1+\gamma)$ percent stratification effect and $50(1-\gamma)$ percent rotation effect. Correspondingly, an overall Nusselt number is defined as the weighted average

$$Nu_\chi = \frac{1+\gamma}{2} Nu_T + \frac{1-\gamma}{2} Nu_\theta, \tag{2.4}$$

of heat and momentum Nusselt numbers, where the weights of heat and momentum transport are proportional to the contributions of the stratification and rotation effect, respectively.

In the special case of $Pr = 1$, we can define a mixed scalar

$$\chi = \frac{1+\gamma}{2} T + \frac{1-\gamma}{2} \theta, \tag{2.5}$$

which has the same boundary condition as those of T and θ. The evolution of T and θ should be very similar because the diffusivity of θ is the same as that of T, and the ensemble average of the source term of θ is $(1-R_\Omega)^{-1}\langle \partial \tilde{p}/\partial x \rangle = 0$. Therefore, it is reasonable to conjecture that $\theta \approx T \approx \chi$ at $Pr = 1$, which we call as the inertial-frame Reynolds analogy. Under such conjecture, the Coriolis and buoyancy term in (2.2*b*) can be approximately unified into an overall buoyancy-like term:

$$R_\Omega(1-R_\Omega)\theta + \frac{Ra}{Re^2 Pr} T \approx \left[R_\Omega(1-R_\Omega) + \frac{Ra}{Re^2 Pr} \right] \chi = Ri_\chi \chi, \tag{2.6}$$

which perfectly demonstrates the adequacy of defining Ri_χ.

Motivated by the mathematical analogy between the Coriolis and buoyancy effects, we propose another compelling conjecture that the heat and momentum Nusselt numbers, Nu_T and Nu_θ, respectively, are primarily governed by the Reynolds number Re and the overall Richardson number Ri_χ, with little sensitivity to γ and Pr. In essence, we anticipate that in the plane Couette system, the Coriolis and buoyancy forces exert nearly identical influences, if not entirely indistinguishable, on both heat and momentum transport. Following the reference of 'the twins' to Taylor–Couette and Rayleigh–Bénard systems (Busse 2012), we call the second conjecture the twin-force analogy.

The piecewise definition of Ri_T is motivated by the twin-force analogy. Such analogy is likely to hold for $Pr = 1$, which means that $Nu_\theta|_{\gamma=-1} = Nu_\chi|_{\gamma=-1} \approx Nu_\chi|_{\gamma=+1} = Nu_T|_{\gamma=+1}$ at $Pr = 1$, and fixed Re and Ri_χ. Since Nu_θ in a rotating plane Couette system ($\gamma = -1$) does not depend on the Prandtl number Pr, it is necessary to make Nu_T in a sheared Rayleigh–Bénard system ($\gamma = +1$) almost independent on Pr to extend the conjecture to systems with $Pr \neq 1$. This requires a proper definition of Ri_T. The results of Blass *et al.* (2021) show that the influence of Pr on heat transport in sheared Rayleigh–Bénard convection is relatively small when $Pr < 1$ and considerable when $Pr > 1$. Furthermore, when $Pr > 1$, the thermal boundary layer should be embedded in the momentum boundary layer in sheared Rayleigh–Bénard convection, which indicates that the influence of viscosity is less important and that Ra can be replaced with $RaPr$ in which ν is absent. The appropriateness of such a definition will be examined by simulation results in the next section.

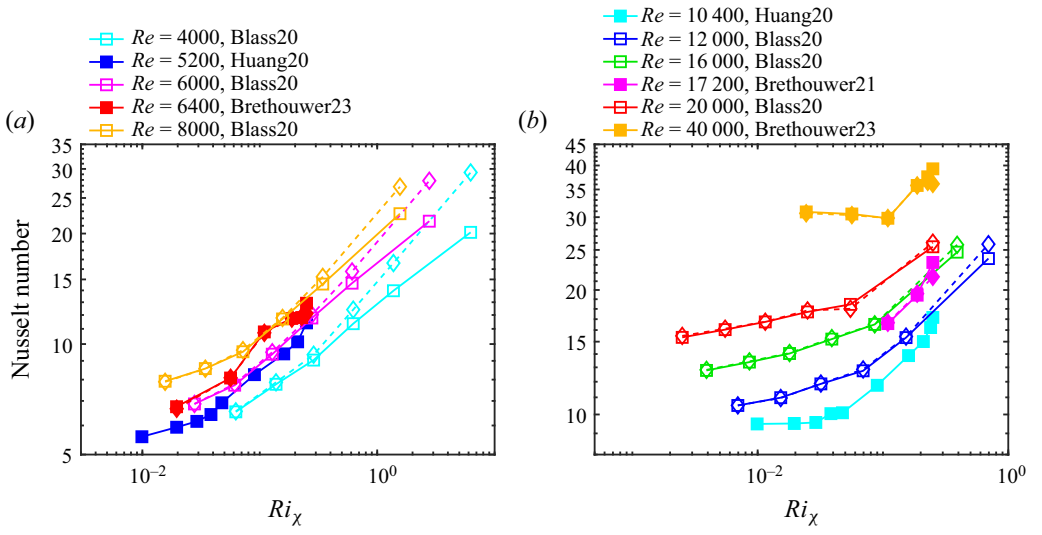

Figure 2. Momentum Nusselt number Nu_θ (□ with solid lines) and heat Nusselt number Nu_T (◇ with dashed lines) as functions of overall Richardson number Ri_χ in both rotating plane Couette flow ($\gamma = -1$, solid symbols) and sheared Rayleigh–Bénard convection ($\gamma = +1$, hollow symbols) at different $Pr = 1$, and (*a*) $Re < 10\,000$ and (*b*) $Re > 10\,000$. Data are from Huang *et al.* (2020), Blass *et al.* (2020), Brethouwer (2021, 2023).

3. Numerical results and discussions

3.1. *Previous results*

Previous studies on rotating plane Couette flow (Bech & Andersson 1996, 1997; Tillmark & Alfredsson 1996; Alfredsson & Tillmark 2005; Tsukahara, Tillmark & Alfredsson 2010; Gai *et al.* 2016; Huang *et al.* 2019; Huang, Xia & Chen 2020; Brethouwer 2021) and sheared Rayleigh–Bénard convection (Blass *et al.* 2020, 2021) may provide some evidence for the validity of our conjectures. Figure 2 shows Nu_θ and Nu_T from direct numerical simulations at different $Re \in [4000, 40\,000]$, $\gamma = \pm 1$ and Ri_χ. The results of rotating plane Couette flow ($\gamma = -1$) at five different Re are from Huang *et al.* (2020) (without heat transfer data) and Brethouwer (2021, 2023), while those of sheared Rayleigh–Bénard convection ($\gamma = +1$) at six different Re are from Blass *et al.* (2020). Different normalized efficiencies of momentum transport (friction Reynolds numbers and rotating-frame momentum Nusselt numbers) are transformed into Nu_θ following the relations derived in Appendix B.

The first apparent phenomenon is that Nu_θ is close to Nu_T in the same case, and the relative difference between them is $O(10\,\%)$ when $Ri_\chi < 0.25$. This strongly supports the validity of the inertial-frame Reynolds analogy (which reduces to the classical Reynolds analogy when $R_\Omega = 0$), as can also be indicated by the analysis of rotating wall turbulence performed by Zhang *et al.* (2019), Brethouwer (2021, 2023). With more detailed observation, it can be seen that the turbulence enhanced by stratification ($\gamma = +1$) is usually more efficient in heat transport than (inertial-frame) momentum transport, and the turbulence enhanced by rotation ($\gamma = -1$) is usually more efficient in momentum transport. Figure 2 also shows that a rotating system and a stratified system at similar Re and Ri_χ would have almost equally similar Nu_θ and Nu_T, which indicates the validity of the twin-force analogy.

Re	Pr	$Ra/10^6$	R_Ω	Ri_χ	γ	Nu_T	Nu_θ	Nu_χ
5000	1	0.00	0.000	0	–	5.02	5.05	5.04
5000	1	−0.50	0.064	0.04	−2	7.01	7.05	7.07
5000	1	0.00	0.042	0.04	−1	7.11	7.13	7.13
5000	1	0.50	0.020	0.04	0	7.04	7.05	7.05
5000	1	1.00	0.000	0.04	1	6.80	6.77	6.80
5000	1	1.50	−0.020	0.04	2	6.55	6.47	6.59
5000	1	−2.00	0.400	0.16	−2	9.30	9.43	9.49
5000	1	0.00	0.200	0.16	−1	10.07	10.12	10.12
5000	1	2.00	0.088	0.16	0	9.78	9.80	9.79
5000	1	4.00	0.000	0.16	1	9.43	9.24	9.43
5000	1	6.00	−0.074	0.16	2	9.09	8.74	9.26
5000	0.25	0.00	0.000	0	–	2.67	5.05	3.86
5000	0.25	−2.00	0.400	0.16	−2	1.49	3.93	5.15
5000	0.25	0.00	0.200	0.16	−1	6.23	10.12	10.12
5000	0.25	2.00	0.088	0.16	0	7.36	11.71	9.53
5000	0.25	4.00	0.000	0.16	1	8.92	13.53	8.92
5000	0.25	6.00	−0.074	0.16	2	10.28	14.75	8.04
5000	4	0.00	0.000	0	–	9.15	5.05	7.10
5000	4	−0.50	0.400	0.16	−2	18.11	10.83	10.17
5000	4	0.00	0.200	0.16	−1	16.45	10.12	10.12
5000	4	0.50	0.088	0.16	0	13.78	8.58	9.62
5000	4	1.00	0.000	0.16	1	9.57	5.37	9.57
5000	4	1.50	−0.074	0.16	2	1.00	1.00	1.00
10 000	1	0.00	0.000	0	–	8.49	8.42	8.45
10 000	1	−8.00	0.400	0.16	−2	13.43	14.32	14.76
10 000	1	0.00	0.200	0.16	−1	13.63	13.54	13.54
10 000	1	8.00	0.088	0.16	0	13.57	13.47	13.52
10 000	1	16.00	0.000	0.16	1	13.59	13.38	13.59
10 000	1	24.00	−0.074	0.16	2	14.72	14.05	15.05

Table 1. Parameters used in the present study, along with the computed heat, momentum and overall Nusselt numbers.

However, figure 2 only supports our conjectures at $Pr = 1$ and $\gamma = \pm 1$, where only one of the rotation and stratification effects appears in each case. Further examinations and discussions for more arbitrary combinations of rotation and stratification in a wide range of Pr should be carried out.

3.2. *Present results*

To quantitatively test our conjectures in more complex conditions, we performed direct numerical simulations using the open-source spectral element code NEK5000 at $Re \in \{5000, 10\,000\}$, $Pr \in \{1, 4^{\pm 1}\}$, $Ri_\chi \in \{0, 0.04, 0.16\}$ and $\gamma \in \{0, \pm 1, \pm 2\}$. The computational domain used in this study is $L_x \times L_y \times L_z = 9\pi \times 1 \times 4\pi$, and it is accompanied by an equivalent grid size $n_x \times n_y \times n_z$ of $568 \times 71 \times 505$ for $Re = 5000$ and $1072 \times 106 \times 617$ for $Re = 10\,000$. More computational set-ups and validation procedures are detailed in Appendix C. Physical parameters, along with the computed heat, momentum and overall Nusselt numbers, are shown in table 1.

Figure 3 shows the heat, momentum and overall Nusselt numbers of plane Couette systems in statistically steady state at $Pr = 1$ and at different values of Re, Ri_χ and γ.

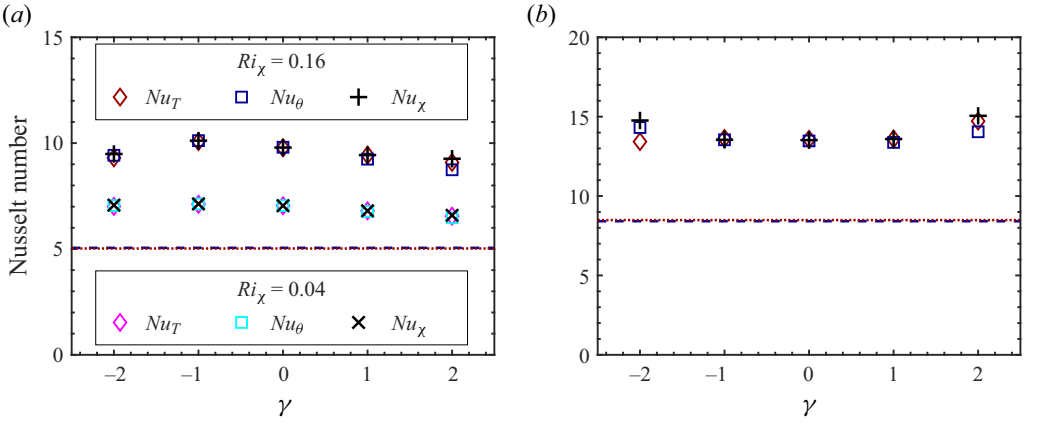

Figure 3. Heat Nusselt number Nu_T, momentum Nusselt number Nu_θ and overall Nusselt number Nu_χ as functions of the overall Richardson number Ri_χ and the relative stratification-rotation difference γ for plane Couette flow at $Pr = 1$, and (*a*) $Re = 5000$ and (*b*) $Re = 10\,000$. The red and blue lines denote the heat and momentum Nusselt numbers, respectively, at the condition of $Ri_T = Ri_\theta = 0$.

It is worth noting that the relative stratification-rotation difference, γ, serves as a useful classification parameter for the system, dividing it into five distinct types: stable stratification and unstable rotation ($\gamma < -1$), purely unstable rotation ($\gamma = -1$), unstable stratification and unstable rotation ($-1 < \gamma < +1$), purely unstable stratification ($\gamma = +1$), and unstable stratification and stable rotation ($\gamma > +1$). Although the large-scale patterns in statistically steady states can be different under different initial conditions, it can be indicated from Huang *et al.* (2019, 2020) that the resulting variations in heat and momentum transfer are usually acceptable in the following discussions. In addition, all cases at the same Re and $Ri_\chi \neq 0$ are initiated with the same velocity and temperature field, which can reduce the difference of flow state between two neighbouring cases with similar γ.

In figure 3, we observe that for $Pr = 1$, the values of Nu_T and Nu_θ are relatively close to each other in the same system. This indicates the validity of our first conjecture in § 2.3, namely the inertial-frame Reynolds analogy, when complex combinations of rotation and stratification are present. The validity of the inertial-frame Reynolds analogy at $R_\Omega \neq 0$ straightforwardly implies the invalidity of the classical Reynolds analogy calculated from rotating-frame momentum transfer (Brethouwer 2018), as indicated by Zhang *et al.* (2019) and Brethouwer (2021, 2023). An explanation based on the Lagrangian view proposed by Zhang *et al.* (2019) is helpful for understanding: under spanwise system rotation, the evolution of the rotating-frame streamwise velocity carried by vertical motions can be written as

$$\frac{\mathrm{d}u}{\mathrm{d}t} \approx R_\Omega v + \zeta = R_\Omega \frac{\mathrm{d}y}{\mathrm{d}t} + \zeta, \tag{3.1}$$

where ζ denotes the contributions from other terms in the momentum equation and could be regarded as a stochastic forcing. In other words, when the Coriolis force is present, the inertial-frame streamwise velocity $u - R_\Omega y$ is much more similar to a temperature field than the rotating-frame streamwise velocity u.

The deviation of Nu_θ and Nu_T from the inertial-frame Reynolds analogy is small, but increases to $O(10\,\%)$ at $Ri_\chi = 0.16$ and $\gamma = \pm 2$ for both $Re = 5000$ and $Re = 10\,000$. There is $Nu_\theta > Nu_T$ when $Ri_\theta > 0 > Ri_T$, and $Nu_T > Nu_\theta$ when $Ri_T > 0 > Ri_\theta$.

This is consistent with the previous simulation results (figure 2). A possible reason is that rotation-induced flow structures are more efficient for momentum transport, while buoyancy-induced flow structures are more efficient for heat transport. The difference in flow structures can be indicated in the difference between the Coriolis and buoyancy effects on vorticity:

$$\boldsymbol{\nabla}\times(R_\Omega\boldsymbol{u}\times\hat{\boldsymbol{z}})\leftrightarrow R_\Omega i\boldsymbol{k}\times(\check{\boldsymbol{u}}\times\hat{\boldsymbol{z}})=iR_\Omega(1-R_\Omega)\left(-k_z\check{\theta},\frac{k_z\check{v}}{1-R_\Omega},\frac{k_z\check{w}}{1-R_\Omega}\right),\tag{3.2a}$$

$$\boldsymbol{\nabla}\times\left(\frac{Ra}{Re^2Pr}T\hat{\boldsymbol{y}}\right)\leftrightarrow i\boldsymbol{k}\times\hat{\boldsymbol{y}}\frac{Ra}{Re^2Pr}\check{T}=i\frac{Ra}{Re^2Pr}(-k_z\check{T},0,k_x\check{T}),\tag{3.2b}$$

where $\boldsymbol{k}=(k_x,k_y,k_z)$ denotes the spatial wavenumber and $\check{\varphi}(\boldsymbol{k})$ denotes the spatial Fourier transform of $\varphi(\boldsymbol{x})$. The last equality of (3.2*a*) is obtained using the incompressible condition $i\boldsymbol{k}\cdot\check{\boldsymbol{u}}=0$ and the fact that $k_z\check{y}\equiv 0$. Therefore, even if $Pr=1$ and $\theta=T$ everywhere, only the streamwise curl of the summed force can be unified into $-Ri_\chi k_z\check{\chi}$.

More importantly, at the same Ri_χ, we find in figure 3 that γ only has very small influence on the three Nusselt numbers, thus verifying the twin-force analogy for $Pr=1$ situations. This indicates that the Coriolis and buoyancy forces have almost the same effect on turbulent transport, especially for purely stratified ($\gamma=+1$) or purely rotating ($\gamma=-1$) cases. Furthermore, they can easily superpose when their Richardson numbers have the same sign ($|\gamma|<1$), and partially counteract when their Richardson numbers have opposite signs ($|\gamma|>1$).

In the case of $Re=5000$ and $Pr=1$, there is a small decrease of both heat and momentum Nusselt numbers for $\gamma\geq-1$. It can be attributed to the suppression effect of wall shear on plumes. By using the variable transformation given in (2.2*a*), the momentum Nusselt number can be related to the normalized average wall shear, which can be called as the rotating-frame momentum Nusselt number and given by

$$\left.\frac{\mathrm{d}\langle u\rangle}{\mathrm{d}y}\right|_{\pm0.5}=Nu_\theta-\frac{1-\sqrt{1-2(1-\gamma)Ri_\chi}}{2}(Nu_\theta-1).\tag{3.3}$$

Therefore, a nearly constant Nu_θ leads to an increase of wall shear with γ, resulting in a stronger suppression effect on plumes and consequently a suppression of heat and momentum transfer. When Re increases to 10 000, the decrease of Nu_T and Nu_θ is almost negligible, indicating that the velocity fluctuations enhanced by wall shear begin to compensate the suppression effect on plume activity. Similar effects of wall shear can be inferred from Blass *et al.* (2020), which shows that Nu_T at fixed Ra first decreases and then increases with increasing Re. At $Re=10\,000$, the deviation from the twin-force analogy becomes relatively larger, which can be observed in the larger Nu_θ at $\gamma=-2$ and the larger Nu_T at $\gamma=2$. This can also be attributed to the differences between the Coriolis and buoyancy effects (3.2) and the specialized transfer characteristics of flow structures.

To further examine or demonstrate the validity of our conjectures for $Pr=1$, the mean velocity profiles $\langle u\rangle$ together with the normalized inertial-frame velocity profiles $\langle\theta\rangle$ at $Re=5000$, $Ri_\chi=0.16$ and $Pr=1$ are shown in figure 4. It can be seen in figure 4(*a*) that $\langle u\rangle$ strongly depends on γ. However, such dependence is mainly due to the velocity transformation relation between the inertial frame and the rotating frame. This is because $\langle\theta\rangle$ at different γ almost coincide, as shown in figure 4(*b*), indicating the validity of the twin-force analogy. Furthermore, within $y\in[-0.3,0.3]$, there is $\langle\theta\rangle\approx0$, which is equivalent to $\langle u\rangle\approx R_\Omega y$ in the rotating frame. The local linear law of $\langle u\rangle$ is

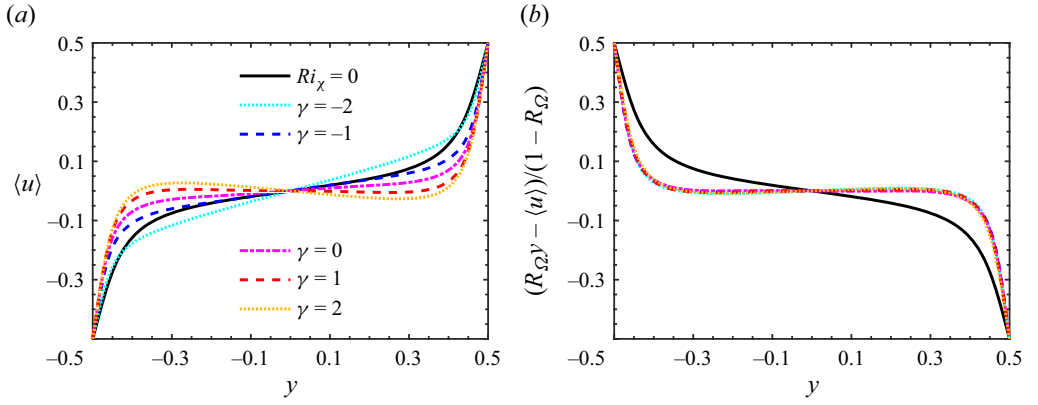

Figure 4. Mean profiles at $Re = 5000$, $Ri_\chi = 0.16$ and $Pr = 1$ of (a) streamwise velocity u and (b) normalized inertial-frame streamwise velocity $\theta = (R_\Omega y - u)/(1 - R_\Omega)$.

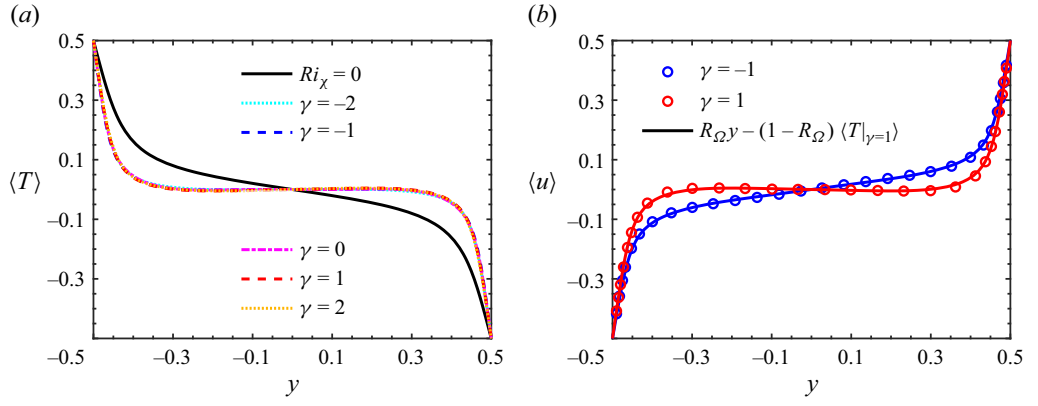

Figure 5. Mean profiles at $Re = 5000$, $Ri_\chi = 0.16$ and $Pr = 1$ of (a) temperature T and (b) velocity u, together with the estimations obtained from the $\langle T \rangle$ in sheared Rayleigh–Bénard convection ($\gamma = +1$).

referred to as the zero mean absolute vorticity state (Hamba 2006; Grundestam, Wallin & Johansson 2008) in spanwise rotating plane Poiseuille turbulence. This behaviour can also be explained using the Lagrangian view (Zhang *et al.* 2019) as briefed in (3.1). A closer observation suggests the non-monotonicity of $\langle \theta \rangle$ at $\gamma = \pm 2$. This is similar to the non-monotonicity of mean temperature profiles in sheared Rayleigh–Bénard convection (Blass *et al.* 2021).

Figure 5(a), demonstrating that the mean temperature profiles at $Re = 5000$, $Ri_\chi = 0.16$ and $Pr = 1$ are almost invariant with γ, also supports the twin-force analogy. To examine the inertial-frame Reynolds analogy, we can examine the accuracy of estimating $\langle u \rangle$ at different γ only with the $\langle T \rangle$ at $\gamma = +1$. Under the assumption that $\langle \theta \rangle \approx \langle T \rangle$, the estimation formula of $\langle u \rangle$ is $R_\Omega y - (1 - R_\Omega)\langle T|_{\gamma=1}\rangle$, where $\langle T|_{\gamma=1}\rangle$ denotes the $\langle T \rangle$ in sheared Rayleigh–Bénard system ($\gamma = +1$) at the same Re and Ri_χ. As shown in figure 5(b), which depicts $\langle u \rangle$ and the corresponding estimations based on $\langle T|_{\gamma=1}\rangle$, the accuracy of the inertial-frame Reynolds analogy is satisfactory. In addition, figure 5(b) also suggests that the inertial-frame Reynolds analogy and the twin-force analogy can help to predict temperature or velocity profiles in complex rotating stratified systems with experimental results in less complex systems.

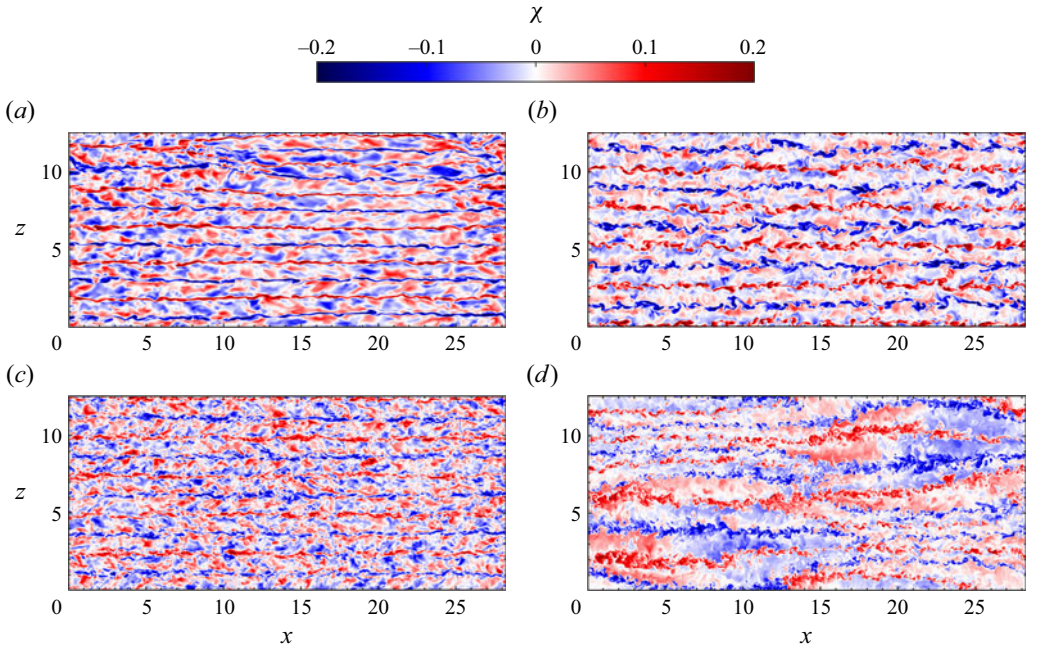

Figure 6. Instantaneous contours of χ in the $y = 0$ plane at $Pr = 1$ and $Ri_\chi = 0.16$: (*a*) $Re = 5000$, $\gamma = -1$; (*b*) $Re = 5000$, $\gamma = +1$; (*c*) $Re = 10\,000$, $\gamma = -1$; (*d*) $Re = 10\,000$, $\gamma = +1$.

Flow structures at $Pr = 1$, $Ri_\chi = 0.16$ and $\gamma = \pm 1$ are visualized in figure 6 with instantaneous contours of χ in the $y = 0$ plane. Notably, the rotating plane Couette flow ($\gamma = -1$) and sheared Rayleigh–Bénard convection ($\gamma = +1$) have not been simultaneously visualized in prior studies. The observed large-scale streak-like structures, known as plume currents (Zhang *et al.* 2022), consist of plumes driven by either stratification or rotation, and drive the large-scale streamwise rolls. A striking similarity emerges when comparing the pure rotating and pure stratified systems at $Re = 5000$. Figure 6(*a*) shows that there can be five pairs ($0 < x < 7$) or six pairs ($10 < x < 25$) of plume currents in the purely rotating case, and figure 6(*b*) shows that there can be five pairs of plume currents in the purely stratified case, indicating a close resemblance between the rotation and stratification effect on large-scale flow structures. It is worth noting that in the current periodic spanwise domain, the number of plume currents may be influenced by initial conditions (Huisman *et al.* 2014; Huang *et al.* 2019, 2020) or could change after extremely long simulation time (Zhang *et al.* 2022). However, usually, the sensitivity to initial condition only allows approximately a relative uncertainty of ± 1 pairs of plume currents. Therefore, the large-scale patterns of the rotating plane Couette and sheared Rayleigh–Bénard systems at $Re = 5000$ and $Pr = 1$ would still be very similar even with possible variations depending on initial conditions. Difference in small-scale fluctuations can be inferred by more detailed observation on figure 6(*a*,*b*): plume currents induced by rotation are relatively narrower and straighter, while those induced by stratification are more chaotic. This can be attributed to the different expressions shown by (3.2) of the Coriolis and buoyancy effects on vorticity. Only the spanwise component of $\boldsymbol{k}$ appears in the Coriolis term, indicating that the self-sustaining process of rotation-induced structures mainly involves spanwise variations. In contrast, both k_x and k_z appear in the buoyancy

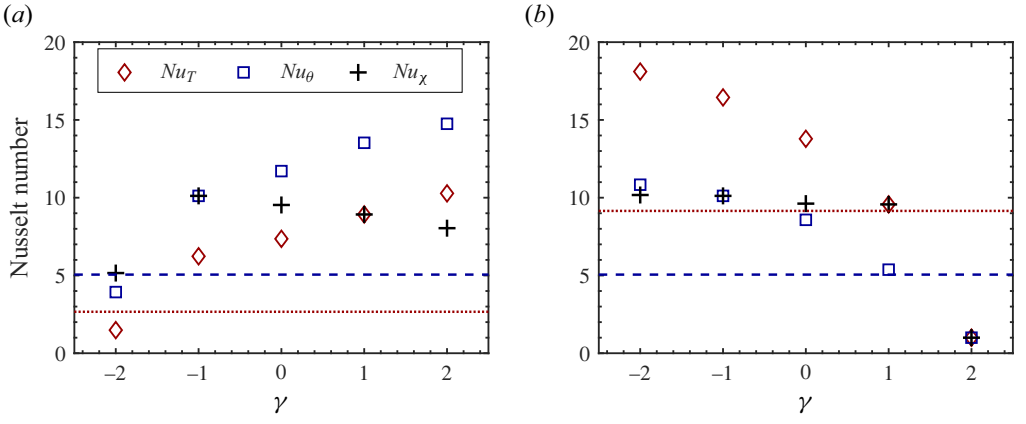

Figure 7. Heat Nusselt number Nu_T, momentum Nusselt number Nu_θ and overall Nusselt number Nu_χ as functions of the relative stratification-rotation difference γ for plane Couette flow at $Re = 5000$, $Ri_\chi = 0.16$, and (*a*) $Pr = 0.25$ and (*b*) $Pr = 4$. The red and blue lines denote the heat and momentum Nusselt numbers, respectively, at the condition of $Ri_T = Ri_\theta = 0$.

term, indicating that the corresponding prevalent flow structures have larger degrees of freedom.

The changes of rotating plane Couette and sheared Rayleigh–Bénard systems under the increase of Re are very different. Figure 6(*c*) shows that there are five pairs of plume currents in the purely rotating case at $Re = 10\,000$, which is similar to the result at $Re = 5000$, except that plume currents become more chaotic and fragmented. In contrast, as shown in figure 6(*d*), the purely stratified case at $Re = 10\,000$ exhibits large streamwise variations of the spanwise distribution of plume currents. The spanwise distance between neighbouring plume currents varies between approximately 0.7 and 3. The primary reason is that larger Re strongly activates the k_x modes, and the distribution of flow structures tends to be more horizontally isotropic, under much weaker constraint on spanwise distance.

In contrast, the resemblance between Taylor–Couette turbulence and Rayleigh–Bénard convection is significantly weaker in terms of flow structures, even when carefully adjusting the parameters to yield similar Nusselt numbers (Brauckmann *et al.* 2017). To elaborate, while the governing equations remain identical in the context of traditional and sheared Rayleigh–Bénard convection, it is only the latter, characterized by wall shear, that engenders the elongated large-scale structures reminiscent of those in Taylor–Couette or rotating plane Couette turbulence. This delineates a pivotal insight: beyond the mathematical affinities elucidated in § 2.2, the consistency of symmetry and wall shear crucially contributes to the striking similarity observed among diverse rotating stratified wall turbulence. These findings provide compelling evidence for a much stronger connection between rotation-driven and stratification-driven dynamics when both are put in the background of wall turbulence.

Figure 7 shows the Nusselt numbers at $Re = 5000$, $Ri_\chi = 0.16$, and different values of γ and $Pr \neq 1$. It can be seen that the behaviour of the heat, momentum and overall Nusselt numbers becomes more intricate as the Prandtl number Pr varies. As shown in figure 7(*a*), for $Pr = 0.25$, the heat Nusselt number is always smaller than the momentum Nusselt number, indicating that the thermal boundary layer is thicker than the momentum boundary layer in the inertial frame. This suggests that stratification has a globally larger influence than rotation in situations where $Pr \ll 1$. As the strength of unstable

stratification increases with increasing γ, the overall enhancement of turbulence by rotation and stratification also increases, leading to an increase in both Nu_T and Nu_θ. At $\gamma = -2$, despite unstable rotation having a characteristic strength three times that of stable stratification, the unstable momentum boundary layer is embedded in the stable thermal boundary layer. This leads to partial laminarization and a significant decrease in both heat and momentum Nusselt numbers.

The results at $Pr = 4$ shown in figure 7(*b*) exhibit a trend that is exactly opposite to that of the $Pr = 0.25$ cases. In this scenario, the momentum boundary layer is thicker than the thermal boundary layer, leading to the dominance of the rotation effect, and causing both Nu_T and Nu_θ to increase as γ decreases (increasing strength of unstable rotation). Notably, at $\gamma = 2$, there is even a complete laminarization observed.

The present results perfectly demonstrated the appropriateness of our definition of Ri_T in § 2.3. It has already been found that the twin-force analogy is valid at $Pr = 1$, and it is obvious that in purely rotating cases ($\gamma = -1$), the $Nu_\chi = Nu_\theta$ is independent to Pr. As shown in table 1, in purely stratified cases ($\gamma = +1$), the $Nu_\chi = Nu_T$ is insensitive to Pr, which aligns with the intended purpose of the piecewise definition of Ri_χ. Consequently, there are six cases at $Re = 5000$, $Ri_\chi = 0.16$ and $\gamma = \pm 1$ that have very similar Nu_χ, which strongly supports the twin-force analogy.

While heat and momentum transport exhibit significant changes with γ for $Pr \neq 1$, the overall Nusselt number Nu_χ at $Re = 5000$ and $Ri_\chi = 0.16$ shows weak dependence on Pr and γ for the cases that are not laminarized (13 out of 15 cases at three Pr). This observation provides compelling evidence for the partial validity of the twin-force analogy across all values of Pr: Nu_χ is mainly determined by Re and Ri_χ, regardless of specific (stable or unstable) contributions from the rotation and stratification effect. In other words, rotation and stratification can serve as approximate substitutes for each other. Although the inertial-frame Reynolds analogy is generally invalid when $Pr \neq 1$, the transport behaviours of the systems can still be interpreted as those controlled by two buoyant scalars with distinct Prandtl or Schmidt numbers (Turner 1979; Yang, Verzicco & Lohse 2016; Garaud 2018).

The present results also indicate the similarity between Taylor–Couette flow and sheared Rayleigh–Bénard convection. We already found that when Re is fixed, rotating plane Couette flow at a rotation number $0 < R_\Omega < 0.5$ is very similar to sheared Rayleigh–Bénard convection at $Pr = 1$ and Ri_T taking the value of $R_\Omega(1 - R_\Omega)$. For the Taylor–Couette system, it is reasonable to choose a rotating frame with angular velocity being the averaged value of the inner and outer cylinder, and define a R_Ω using this angular velocity (Dubrulle *et al.* 2005; Brauckmann *et al.* 2016). Furthermore, Dubrulle *et al.* (2005) demonstrated that Taylor–Couette and plane Couette systems, when at the same Re and R_Ω, exhibit significant similarities, especially when $\eta > 0.71$. For classical Taylor–Couette systems with fixed outer cylinder, the definition of rotation number becomes $R_\Omega = 1 - \eta$. Therefore, it is reasonable to anticipate that a Taylor–Couette system with radius ratio $\eta > 1/2$ and fixed outer cylinder exhibits strong similarity to sheared Rayleigh–Bénard convection at Ri_T being $R_\Omega(1 - R_\Omega) = (1 - \eta)[1 - (1 - \eta)] = \eta(1 - \eta)$.

4. Conclusion

Our study has investigated the effects of rotation (Coriolis force) and stratification (buoyancy force) on plane Couette turbulence both separately and in combination. Previous and present simulation results indicate the validity of the twin-force analogy signifying that the Coriolis and buoyancy forces are ‘twin forces’ whose effects can

be unified. Specifically, in turbulent cases at fixed Re and Pr, the overall Nusselt number Nu_χ is primarily determined by the total strength of rotation and stratification characterized by the overall Richardson number Ri_χ, which can be achieved by considerably arbitrary combinations of stratification and rotation. In the special case of $Pr = 1$, large-scale flow structures driven by the buoyancy force are remarkably similar to those driven by the Coriolis force. In addition, the inertial-frame Reynolds analogy, standing for the approximate coincidence of heat and inertial-frame momentum transfer at $Pr = 1$, is also valid. Building on these discoveries, we further conjecture that the ultimate Taylor–Couette turbulence with radius ratio $\eta > 1/2$ and a fixed outer cylinder is nearly equivalent to high-Reynolds-number sheared Rayleigh–Bénard convection at $Pr = 1$ and Ri_T being $\eta(1-\eta)$, rather than the classical Rayleigh–Bénard convection.

Funding. This work is financially supported by the Natural Science Foundation of China (grant nos 11988102, 12302284) and the Ningbo Science and Technology Bureau (grant no. 2023Z227).

Declaration of interests. The authors report no conflict of interest.

Author ORCIDs.
Shengqi Zhang https://orcid.org/0000-0001-8273-7484;
Chao Sun https://orcid.org/0000-0002-0930-6343.

Appendix A. Derivations of (2.2)

The streamwise and wall-normal components of the momentum equation (2.1*b*) are

$$\frac{\partial u}{\partial t} + \boldsymbol{u}\cdot\boldsymbol{\nabla} u = -\frac{\partial p}{\partial x} + \frac{1}{Re}\nabla^2 u + R_\Omega v, \tag{A1a}$$

$$\frac{\partial v}{\partial t} + \boldsymbol{u}\cdot\boldsymbol{\nabla} v = -\frac{\partial p}{\partial y} + \frac{1}{Re}\nabla^2 v - R_\Omega u + \frac{Ra}{Re^2 Pr}T. \tag{A1b}$$

By introducing $\theta = (R_\Omega y - u)/(1 - R_\Omega)$, the Coriolis term in (A1*b*) can be written as

$$\begin{aligned} -R_\Omega u\hat{\boldsymbol{y}} &= -R_\Omega[R_\Omega y - (1-R_\Omega)\theta]\hat{\boldsymbol{y}} \\ &= R_\Omega(1-R_\Omega)\theta\hat{\boldsymbol{y}} - R_\Omega^2 y\hat{\boldsymbol{y}} \\ &= R_\Omega(1-R_\Omega)\theta\hat{\boldsymbol{y}} - \boldsymbol{\nabla}\frac{R_\Omega^2 y^2}{2}, \end{aligned} \tag{A2}$$

where the last gradient term can be absorbed into a redefined pressure $\tilde{p} = p + R_\Omega^2 y^2/2$. The evolution of $\theta = (R_\Omega y - u)/(1 - R_\Omega)$ can be derived from (A1*a*):

$$\begin{aligned} \frac{\partial\theta}{\partial t} + \boldsymbol{u}\cdot\boldsymbol{\nabla}\theta &= \frac{\partial}{\partial t}\frac{R_\Omega y - u}{1-R_\Omega} + \boldsymbol{u}\cdot\boldsymbol{\nabla}\frac{R_\Omega y - u}{1-R_\Omega} \\ &= \frac{1}{1-R_\Omega}\left(-\frac{\partial u}{\partial t} + R_\Omega\boldsymbol{u}\cdot\hat{\boldsymbol{y}} - \boldsymbol{u}\cdot\boldsymbol{\nabla}u\right) \\ &= \frac{1}{1-R_\Omega}\left[R_\Omega v - \left(\frac{\partial u}{\partial t} + \boldsymbol{u}\cdot\boldsymbol{\nabla}u\right)\right] \\ &= \frac{1}{1-R_\Omega}\left[R_\Omega v - \left(-\frac{\partial p}{\partial x} + \frac{1}{Re}\nabla^2 u + R_\Omega v\right)\right] \end{aligned}$$

$$= \frac{1}{1-R_\Omega}\left(\frac{\partial p}{\partial x} - \frac{1}{Re}\nabla^2 u\right)$$
$$= \frac{1}{1-R_\Omega}\frac{\partial \tilde{p}}{\partial x} + \frac{1}{Re}\nabla^2\theta. \tag{A3}$$

Appendix B. Relations between normalized efficiencies of momentum transport

The rotating-frame momentum Nusselt number Nu_m (Brethouwer 2021, 2023), the present (inertial-frame) momentum Nusselt number Nu_θ and the friction Reynolds number Re_τ are normalized indicators of streamwise momentum transport efficiency. With dimensional constants and variables, they can be written as

$$Nu_m = \left.\frac{\mathrm{d}\langle u\rangle/\mathrm{d}y}{[U]/H}\right|_{\pm H/2}, \quad Nu_\theta = \left.\frac{\mathrm{d}\langle\theta\rangle/\mathrm{d}y}{[\theta]/H}\right|_{\pm H/2}, \quad Re_\tau = \frac{u_\tau H}{\nu}, \tag{B1a,b}$$

where

$$\theta = \frac{2\Omega y - u}{1-R_\Omega}, \quad [\theta] = \theta|_{+H/2} - \theta|_{-H/2}, \quad u_\tau = \sqrt{\nu\left.\frac{\mathrm{d}\langle u\rangle}{\mathrm{d}y}\right|_{\pm H/2}}. \tag{B2a–c}$$

It can be seen with simple derivations that Nu_θ can be expressed with Nu_m or Re_τ when $R_\Omega \neq 1$:

$$Nu_\theta = \frac{2\Omega - \mathrm{d}\langle u\rangle/\mathrm{d}y}{2\Omega - [U]/H} = \begin{cases} \dfrac{2\Omega - Nu_m[U]/H}{2\Omega - 2\Omega/R_\Omega} = \dfrac{Nu_m - R_\Omega}{1-R_\Omega} \\ \dfrac{2\Omega - Re_\tau^2\nu/H^2}{2\Omega - 2\Omega/R_\Omega} = \dfrac{Re^{-1}Re_\tau^2 - R_\Omega}{1-R_\Omega} \end{cases}. \tag{B3}$$

Appendix C. Computational domain and grid quality

NEK5000 has been thoroughly validated for simulating turbulent Rayleigh–Bénard convection, as reported by Chandra & Verma (2013) and Kooij *et al.* (2018). The computational domain $L_x \times L_y \times L_z = 9\pi \times 1 \times 4\pi$ is large enough to capture the spanwise distribution and streamwise meandering of the large-scale streamwise structures observed in sheared Rayleigh–Bénard convection (Blass *et al.* 2020) and rotating plane Couette flow (Huang *et al.* 2019). The spectral-element grid size $N_x \times N_y \times N_z$ is $81 \times 10 \times 72$ for $Re = 5000$ and $153 \times 15 \times 88$ for $Re = 10\,000$. With 7th-order Legendre polynomials, the spectral-element grid sizes are equivalent to grid size $n_x \times n_y \times n_z$ of $568 \times 71 \times 505$ for $Re = 5000$ and $1072 \times 106 \times 617$ for $Re = 10\,000$. Near-wall refinements are also made to resolve the thermal and momentum boundary layers. The global grid density for $Re = 5000$ is consistent with previous simulations of rotating plane Couette flow at $Re = 5200$ using second-order finite difference (Bech & Andersson 1996, 1997) or pseudo-spectral method (Gai *et al.* 2016; Huang *et al.* 2019). In particular, at a large $Ri_\theta = 0.218$ with the aforementioned grid density and a computational domain of $4\pi \times 1 \times 2\pi$, the computed value of Re_τ is 199.4, which is in excellent agreement with the result of 199.2 obtained by the pseudo-spectral method (Gai *et al.* 2016). These results validate both the NEK5000 code and the present grid density for the simulation of rotating plane Couette flow.

A grid convergence study was performed on a smaller computational domain with dimensions of $L_x \times L_y \times L_z = \pi \times 1 \times 0.5\pi$. The physical and numerical parameters

Re	Ri_χ	Pr	γ	L_x/π	L_z/π	N_x	N_y	N_z	Nu_T	Nu_θ	err[Nu_T]	err[Nu_θ]
5000	0.16	0.25	−1	1	0.5	6	7	6	6.14	10.09	−0.16 %	−0.17 %
5000	0.16	0.25	−1	1	0.5	9	10	9	6.15	10.09	−0.06 %	−0.16 %
5000	0.16	0.25	−1	1	0.5	13	15	13	6.15	10.11	–	–
5000	0.16	0.25	1	1	0.5	6	7	6	9.74	12.21	2.64 %	2.84 %
5000	0.16	0.25	1	1	0.5	9	10	9	9.52	11.93	0.33 %	0.51 %
5000	0.16	0.25	1	1	0.5	13	15	13	9.49	11.87	–	–
5000	0.16	4	−1	1	0.5	6	7	6	16.58	10.09	0.11 %	−0.17 %
5000	0.16	4	−1	1	0.5	9	10	9	16.57	10.12	0.06 %	0.10 %
5000	0.16	4	−1	1	0.5	13	15	13	16.56	10.11	–	–
5000	0.16	4	1	1	0.5	6	7	6	9.67	5.41	0.69 %	0.44 %
5000	0.16	4	1	1	0.5	9	10	9	9.61	5.38	0.06 %	−0.05 %
5000	0.16	4	1	1	0.5	13	15	13	9.60	5.38	–	–
10 000	0.16	1	−1	1	0.5	6	7	6	14.34	14.28	1.53 %	1.87 %
10 000	0.16	1	−1	1	0.5	9	10	9	14.03	13.94	−0.63 %	−0.55 %
10 000	0.16	1	−1	1	0.5	13	15	13	14.12	14.02	–	–
10 000	0.16	1	1	1	0.5	6	7	6	13.94	13.59	4.30 %	4.77 %
10 000	0.16	1	1	1	0.5	9	10	9	13.42	13.03	0.38 %	0.48 %
10 000	0.16	1	1	1	0.5	13	15	13	13.37	12.97	–	–

Table 2. Parameters for the grid convergence study, along with the computed Nusselt numbers and their corresponding relative errors.

used are presented in table 2, where the relative error with respect to the largest grid size at the same physical parameters is denoted by err[·]. It seems that $9 \times 10 \times 9$ spectral elements are sufficient for the small domain size, with relative errors of the heat and momentum Nusselt numbers below 0.65 %. However, flow visualizations at $Re = 10\,000$ show that the corresponding grid density would cause non-physical ripples near the interfaces between elements, even though the Nusselt numbers are well predicted. By further testing on $Re = 10\,000$ cases, we found that $17 \times 15 \times 11$ spectral elements can visually eliminate the ripples in the small domain. Therefore, in accordance with the satisfactory grid density in the small domain, the spectral-element grid size for the large domain is $81 \times 10 \times 72$ for $Re = 5000$ and increased to $153 \times 15 \times 88$ for $Re = 10\,000$.

References

Ahlers, G., Grossmann, S. & Lohse, D. 2009 Heat transfer and large scale dynamics in turbulent Rayleigh-Bénard convection. *Rev. Mod. Phys.* **81** (2), 503–537.

Alfredsson, P.H. & Tillmark, N. 2005 Instability, transition and turbulence in plane Couette flow with system rotation. In *IUTAM Symposium on Laminar-Turbulent Transition and Finite Amplitude Solutions*, pp. 173–193. Springer.

Bech, K.H. & Andersson, H.I. 1996 Secondary flow in weakly rotating turbulent plane Couette flow. *J. Fluid Mech.* **317**, 195–214.

Bech, K.H. & Andersson, H.I. 1997 Turbulent plane Couette flow subject to strong system rotation. *J. Fluid Mech.* **347**, 289–314.

Blass, A., Tabak, P., Verzicco, R., Stevens, R.J.A.M. & Lohse, D. 2021 The effect of Prandtl number on turbulent sheared thermal convection. *J. Fluid Mech.* **910**, A37.

Blass, A., Zhu, X., Verzicco, R., Lohse, D. & Stevens, R.J.A.M. 2020 Flow organization and heat transfer in turbulent wall sheared thermal convection. *J. Fluid Mech.* **897**, A22.

Boussinesq, J. 1903 *Théorie analytique de la chaleur mise en harmonic avec la thermodynamique et avec la théorie mécanique de la lumière: Tome I-[II]*, vol. 2. Gauthier-Villars.

BRADSHAW, P. 1969 The analogy between streamline curvature and buoyancy in turbulent shear flow. *J. Fluid Mech.* **36** (1), 177–191.
BRAUCKMANN, H.J., ECKHARDT, B. & SCHUMACHER, J. 2017 Heat transport in Rayleigh–Bénard convection and angular momentum transport in Taylor–Couette flow: a comparative study. *Phil. Trans. R. Soc.* A **375** (2089), 20160079.
BRAUCKMANN, H.J., SALEWSKI, M. & ECKHARDT, B. 2016 Momentum transport in Taylor–Couette flow with vanishing curvature. *J. Fluid Mech.* **790**, 419–452.
BRETHOUWER, G. 2018 Passive scalar transport in rotating turbulent channel flow. *J. Fluid Mech.* **844**, 297–322.
BRETHOUWER, G. 2021 Much faster heat/mass than momentum transport in rotating Couette flows. *J. Fluid Mech.* **912**, A31.
BRETHOUWER, G. 2023 Strong dissimilarity between heat and momentum transfer in rotating Couette flows. *Intl J. Heat Mass Transfer* **205**, 123920.
BUSSE, F.H. 2012 The twins of turbulence research. *Physics* **5** (4), 1–3.
CHANDRA, M. & VERMA, M.K. 2013 Flow reversals in turbulent convection via vortex reconnections. *Phys. Rev. Lett.* **110** (11), 114503.
DEUSEBIO, E., CAULFIELD, C.P. & TAYLOR, J.R. 2015 The intermittency boundary in stratified plane Couette flow. *J. Fluid Mech.* **781**, 298–329.
DUBRULLE, B., DAUCHOT, O., DAVIAUD, F., LONGARETTI, P.Y., RICHARD, D. & ZAHN, J.P. 2005 Stability and turbulent transport in Taylor–Couette flow from analysis of experimental data. *Phys. Fluids* **17** (9), 095103.
ECKHARDT, B., DOERING, C.R. & WHITEHEAD, J.P. 2020 Exact relations between Rayleigh–Bénard and rotating plane Couette flow in two dimensions. *J. Fluid Mech.* **903**, R4.
FAISST, H. & ECKHARDT, B. 2000 Transition from the Couette–Taylor system to the plane Couette system. *Phys. Rev.* E **61** (6), 7227–7230.
GAI, J., XIA, Z., CAI, Q. & CHEN, S. 2016 Turbulent statistics and flow structures in spanwise-rotating turbulent plane Couette flows. *Phys. Rev. Fluids* **1** (5), 054401.
GARAUD, P. 2018 Double-diffusive convection at low Prandtl number. *Annu. Rev. Fluid Mech.* **50**, 275–298.
VAN GILS, D.P.M., HUISMAN, S.G., BRUGGERT, G.-W., SUN, C. & LOHSE, D. 2011 Torque scaling in turbulent Taylor–Couette flow with co-and counterrotating cylinders. *Phys. Rev. Lett.* **106** (2), 024502.
GROSSMANN, S. & LOHSE, D. 2011 Multiple scaling in the ultimate regime of thermal convection. *Phys. Fluids* **23** (4), 045108.
GROSSMANN, S., LOHSE, D. & SUN, C. 2016 High-Reynolds number Taylor–Couette turbulence. *Annu. Rev. Fluid Mech.* **48**, 53–80.
GRUNDESTAM, O., WALLIN, S. & JOHANSSON, A.V. 2008 Direct numerical simulations of rotating turbulent channel flow. *J. Fluid Mech.* **598**, 177–199.
HAGHSHENAS, A. & MELLADO, J.P. 2019 Characterization of wind-shear effects on entrainment in a convective boundary layer. *J. Fluid Mech.* **858**, 145–183.
HAMBA, F. 2006 The mechanism of zero mean absolute vorticity state in rotating channel flow. *Phys. Fluids* **18** (12), 125104.
HAN, J.-C. 2018 Advanced cooling in gas turbines 2016 Max Jakob memorial award paper. *Trans. ASME J. Heat Transfer* **140** (11), 113001.
HARTMANN, D.L., MOY, L.A. & FU, Q. 2001 Tropical convection and the energy balance at the top of the atmosphere. *J. Clim.* **14** (24), 4495–4511.
HUANG, Y., XIA, Z. & CHEN, S. 2020 Hysteresis behaviour in spanwise rotating plane Couette flow at $Re_w = 2600$. *J. Turbul.* **16**, 1–13.
HUANG, Y., XIA, Z., WAN, M., SHI, Y. & CHEN, S. 2019 Hysteresis behavior in spanwise rotating plane Couette flow with varying rotation rates. *Phys. Rev. Fluids* **4** (5), 052401.
HUISMAN, S.G., VAN GILS, D.P.M., GROSSMANN, S., SUN, C. & LOHSE, D. 2012 Ultimate turbulent Taylor–Couette flow. *Phys. Rev. Lett.* **108** (2), 024501.
HUISMAN, S.G., VAN DER VEEN, R.C., SUN, C. & LOHSE, D. 2014 Multiple states in highly turbulent Taylor–Couette flow. *Nat. Commun.* **5** (1), 1–5.
JEFFREYS, H. 1928 Some cases of instability in fluid motion. *Proc. R. Soc. Lond. Ser.* A **118** (779), 195–208.
JIANG, H., WANG, D., LIU, S. & SUN, C. 2022 Experimental evidence for the existence of the ultimate regime in rapidly rotating turbulent thermal convection. *Phys. Rev. Lett.* **129** (20), 204502.
KADER, B.A. & YAGLOM, A.M. 1990 Mean fields and fluctuation moments in unstably stratified turbulent boundary layers. *J. Fluid Mech.* **212**, 637–662.

KOOIJ, G.L., BOTCHEV, M.A., FREDERIX, E.M.A., GEURTS, B.J., HORN, S., LOHSE, D., VAN DER POEL, E.P., SHISHKINA, O., STEVENS, R.J.A.M. & VERZICCO, R. 2018 Comparison of computational codes for direct numerical simulations of turbulent Rayleigh-Bénard convection. *Comput. Fluids* **166**, 1–8.

KRAICHNAN, R.H. 1962 Turbulent thermal convection at arbitrary Prandtl number. *Phys. Fluids* **5** (11), 1374–1389.

LEZIUS, D.K. & JOHNSTON, J.P. 1976 Roll-cell instabilities in rotating laminar and turbulent channel flows. *J. Fluid Mech.* **77** (1), 153–174.

LOHSE, D. & XIA, K.-Q. 2010 Small-scale properties of turbulent Rayleigh–Bénard convection. *Annu. Rev. Fluid Mech.* **42**, 335–364.

LUTGENS, F.K., TARBUCK, E.J. & TASA, D.G. 2007 *The Atmosphere: An Introduction to Meteorology*. Pearson.

MONIN, A.S. & OBUKHOV, A.M. 1954 Basic laws of turbulent mixing in the surface layer of the atmosphere. *Trans. Geophys. Inst. Acad. Sci. USSR* **151** (163), e187.

OBUKHOV, A. 1946 Turbulence in thermally inhomogeneous atmosphere. *Trudy Inst. Teor. Geofiz. Akad. Nauk SSSR* **1**, 95–115.

OSTILLA-MÓNICO, R., VAN DER POEL, E.P., VERZICCO, R., GROSSMANN, S. & LOHSE, D. 2014 Exploring the phase diagram of fully turbulent Taylor–Couette flow. *J. Fluid Mech.* **761**, 1–26.

PIROZZOLI, S., BERNARDINI, M., VERZICCO, R. & ORLANDI, P. 2017 Mixed convection in turbulent channels with unstable stratification. *J. Fluid Mech.* **821**, 482–516.

PRANDTL, L. 1932 Meteorogische an wendung der stromungslehre. *Beitr. Phys. Atomos.* **19**, 188–202.

SCHUMACHER, J. & SREENIVASAN, K.R. 2020 Colloquium: unusual dynamics of convection in the Sun. *Rev. Mod. Phys.* **92** (4), 041001.

TANAKA, M., KIDA, S., YANASE, S. & KAWAHARA, G. 2000 Zero-absolute-vorticity state in a rotating turbulent shear flow. *Phys. Fluids* **12** (8), 1979–1985.

TAYLOR, G.I. 1923 Stability of a viscous liquid contained between two rotating cylinders. *Phil. Trans. R. Soc. Lond. Ser.* A **223** (605-615), 289–343.

TILLMARK, N. & ALFREDSSON, P.H. 1996 *Experiments on Rotating Plane Couette Flow*, pp. 391–394. Springer.

TSUKAHARA, T., TILLMARK, N. & ALFREDSSON, P.H. 2010 Flow regimes in a plane Couette flow with system rotation. *J. Fluid Mech.* **648**, 5–33.

TURNER, J.S. 1979 *Buoyancy Effects in Fluids*. Cambridge University Press.

VERONIS, G. 1970 The analogy between rotating and stratified fluids. *Annu. Rev. Fluid Mech.* **2** (1), 37–66.

WANG, B.-F., ZHOU, Q. & SUN, C. 2020 Vibration-induced boundary-layer destabilization achieves massive heat-transport enhancement. *Sci. Adv.* **6** (21), eaaz8239.

WYNGAARD, J.C. 1992 Atmospheric turbulence. *Annu. Rev. Fluid Mech.* **24** (1), 205–234.

YANG, Y., VERZICCO, R. & LOHSE, D. 2016 Vertically bounded double diffusive convection in the finger regime: comparing no-slip versus free-slip boundary conditions. *Phys. Rev. Lett.* **117** (18), 184501.

YOU, R., LI, H., TAO, Z. & WEI, K. 2018 Measurement of the mean flow field in a smooth rotating channel with Coriolis and buoyancy effects. *J. Turbomach.* **140** (4), 041002.

YOUNG, R.M.B. & READ, P.L. 2017 Forward and inverse kinetic energy cascades in Jupiter's turbulent weather layer. *Nat. Phys.* **13** (11), 1135–1140.

ZHANG, S., XIA, Z. & CHEN, S. 2022 Flow structures in spanwise rotating plane Poiseuille flow based on thermal analogy. *J. Fluid Mech.* **933**, A24.

ZHANG, S., XIA, Z., SHI, Y. & CHEN, S. 2019 A two-dimensional-three-component model for spanwise rotating plane Poiseuille flow. *J. Fluid Mech.* **880**, 478–496.

ZHOU, Q., TAYLOR, J.R. & CAULFIELD, C.-C.P. 2017 Self-similar mixing in stratified plane Couette flow for varying Prandtl number. *J. Fluid Mech.* **820**, 86–120.

ZHU, X., STEVENS, R.J.A.M., SHISHKINA, O., VERZICCO, R. & LOHSE, D. 2019 $Nu \sim Ra^{1/2}$ scaling enabled by multiscale wall roughness in Rayleigh–Bénard turbulence. *J. Fluid Mech.* **869**, R4.

ZHU, X., VERSCHOOF, R.A., BAKHUIS, D., HUISMAN, S.G., VERZICCO, R., SUN, C. & LOHSE, D. 2018 Wall roughness induces asymptotic ultimate turbulence. *Nat. Phys.* **14** (4), 417–423.